Understanding the Aeroacoustic Radiation Sources and Mechanism in High-Speed Jets

Dissertation

Presented in Partial Fulfillment of the Requirements for the Degree Doctor of Philosophy in the Graduate School of The Ohio State University

By

Michael Crawley, B.S.

Graduate Program in Department of Mechanical Engineering

The Ohio State University

2015

Dissertation Committee:

Mo Samimy, Advisor

Datta Gaitonde

James Gregory

Mei Zhuang

Abstract

Who reads a dissertation abstract?

This work is dedicated to Science . . .

Acknowledgments

I should probably acknowledge someone here . . .

Vita

September 10, 1986 ....Born - Plano, Texas

2009 ......................................B.S. Mechanical Engineering,
University of Texas, Austin.

2009-present ....Graduate Research Associate,
The Ohio State University.

Publications

Research Publications

M. Crawley, C.-W. Kuo, and M. Samimy, "Identification of the Acoustic Response in the Irrotational Near-field of an Excited Subsonic Jet." submitted to *International Journal of Aeroacoustics.*

M. Crawley, R. Speth, D. V. Gaitonde, and M. Samimy, "A Study of the Noise Source Mechanisms in an Excited Mach 0.9 Jet - Complementary Experimental and Computational Analysis." AIAA Paper 2015-0736, *53rd AIAA Aerospace Sciences Meeting.*

M. Crawley, A. Sinha, and M. Samimy, "Near-field and Acoustic Far-field Response of a High-Speed Jet Forced with Plasma Actuators." *AIAA Journal*, expected 2015.

M. Crawley and M. Samimy, "Decomposition of the Near-Field Pressure in an Excited Subsonic Jet." AIAA Paper 2014-2342, *20th AIAA/CEAS Aeroacoustics Conference.*

M. Crawley, A. Sinha, and M. Samimy, "Near-field Pressure and Far-field Acoustic Response of Forced High-Speed Jets." AIAA Paper 2014-0527, *52nd AIAA Aerospace Sciences Meeting.*

M. Crawley, H. Alkandry, A. Sinha, and M. Samimy, "Correlation of Irrotational Near-Field Pressure and Far-Field Acoustic in Forced High-Speed Jets." AIAA Paper 2013-2188, *19th AIAA/CEAS Aeroacoustics Conference.*

H. Alkandry, **M. Crawley**, A. Sinha, M. Kearney-Fischer, and M. Samimy, "An Investigation of the Irrotational Near Field of an Excited High-Speed Jet." AIAA Paper 2013-0325, *51st AIAA Aerospace Sciences Meeting.*

M. Crawley, M. Kearney-Fischer, and M. Samimy, "Control of a Supersonic Rectangular Jet Using Plasma Actuators." AIAA Paper 2012-2211, *18th AIAA/CEAS Aeroacoustics Conference.*

Fields of Study

Major Field: Mechanical Engineering

Studies in: High-speed Jets, Aeroacoustics, Flow Control, Fluid Mechanics, Optical Diagnostics, Wavelets, Machine Learning

Contents

List of Tables

List of Figures

Chapter 1: Introduction

1.1   Motivation

The advent of the turbojet engine led to a transformation in both commercial and military aviation, allowing for much faster flight than previously possible with propellor-driven aircraft. However, the increased thrust of turbojets has come at great cost; significant acoustic radiation is generated by the rotating components (compressor, turbine, fan), by the combustion process, and ultimately by the free jet itself. On the commercial side, the escalating number of flights, encroachment of urban and residential areas near airports, and tightening of environmental regulations have combined to force airports to institute curfews, surcharges and flight path restrictions to combat noise pollution. For the military, hearing damage inflicted on nearby personnel (particularly flight deck crew on aircraft carriers) has necessitated the implementation of noise reduction concepts on tactical aircraft. During takeoff and landing, when acoustic radiation is most problematic to ground crew and surrounding urban and residential areas, the dominant noise source of the jet engine is the aeroacoustic radiation generated by the high velocity engine exhaust. This has spurred extensive research, spanning over six decades, into the acoustic source mechanism in high speed, high Reynolds number jets.

While progress has been made in the field of aeroacoustics, both experimentally [1–3] as well as theoretically [4], understanding of jet noise sources and their radiation mechanisms remains incomplete [5]. This is due to the large number of interrelated parameters (e.g. Reynolds number, temperature ratio, acoustic Mach number, nozzle geometry, et cetera) as well as the large disparity in the associated length and time scales of the turbulent phenomena and the radiated noise. Simulations of controlled free shear layers have suggested that there is significant potential for noise reduction, on the order of 11 dB in some cases [Wei 2006]. However, these simulations relied on non-physically defined actuation (that is, forcing was applied over a defined region by arbitrary energy, momentum, and body force terms), and a physical interpretation of the optimum forcing parameters was not immediately clear to the researchers. Current noise-mitigation technologies for free jets have largely been applied in an adhoc fashion, due to our incomplete understanding of the aeroacoustic sources. Fully realizing this maximum noise reduction potential will require a much more detailed understanding of the mechanism (or mechanisms) by which free jets radiate to the far-field.

It is generally agreed that the dominant noise sources are related to the large-scale turbulent structures present in the mixing layer of the jet. What remains to be determined is what aspects of the large-scale structure evolution and interactions are relevant to the noise generation process. Theoretical models of spatially- and temporally-modulated coherent structures have shown great promise in replicating the observed characteristics of the dominant far-field noise [Cavalieri/Jordan?]. However, direct experimental data linking this structure evolution to the acoustic emission is still lacking. It is on this vein that the current work is focused. Until

recently, experimental data acquisition techniques have been unable to capture the flow physics with enough fidelity (lacking in either spatial or temporal resolution) in order to accurately model the large-scale structures and aeroacoustic sources. By combining contemporary data acquisition methods (free-field microphones and non-time-resolved particle image velocimetry) with novel post-processing algorithms this work aims to directly link the relevant vortex dynamics of the large-scale structures to the acoustic emission events, and in the process identify a simplified aeroacoustic source mechanism.

1.2 Background

1.2.1 Flow Control

Controlling the development of the jet plume, and hence controlling the rate of mixing or intensity and characteristics of the emitted acoustic radiation, is a long running goal of the aeroacoustic community. Passive, permanent modifications to the nozzle have been shown to be quite adept at this task; some examples of these include tabs [citations] and chevrons [citations]. These work to generate counter-rotating streamwise vortices in the developing shear layer, which serve to substantially increase mixing between the core and coflow in the near-nozzle region and ultimately retard the growth of large-scale axisymmetric structures [citation].

Unfortunately, these passive modifications have associated penalties to the engine performance, in terms of added weight or reduced thrust. Due to the passive nature of the flow modification, these performance penalties are in effect over the entire duration of the flight regardless of whether or not the noise reduction is needed. To improve engine efficiency, active control techniques are desired, since they can

be activated when needed, such as during takeoff and landing, and deactivated when unneeded, such as after a commercial airliner reaches cruising altitude. Active control techniques, which seek to manipulate instabilities in the jet shear layer, have been extensively studied in low-speed, low-Reynolds number jets, the most common of which is acoustic drivers [citations]. However, as the speed and Reynolds number of the jet is increased (to match those in practical applications), so too does the required bandwidth and energy of the active drivers. Hence, acoustic or magneto-hydrodynamic drivers lose control authority in these regimes, and more powerful actuators are required.

The last decade has seen a rapid growth in the development of plasma actuators for use in high-speed flow control; though as of yet they have not progressed past the experimental phase. Localized arc filament plasma actuators (LAFPAs) are one such class of plasma actuator, which were developed by a collaboration between the Gas Dynamics and Turbulence Laboratory (GDTL) and the Non-Equilibrium Thermodynamics Laboratory (NETL) at the Ohio State University. LAFPAs can provide the high-amplitude and high-frequency excitation required for control of high Mach number and high Reynolds number jets [citations]. GDTL has used these actuators for noise mitigation and flow control in Mach 0.9 [citations], Mach 1.3 [citations] and Mach 1.65 [citations] jets (both heated and unheated). A review of the development of LAFPAs and their use in flow control and fluid phenomena research in high speed, high Reynolds number jets can be found in Samimy et al. [citation]. More recently, the diagnostic potential of LAFPAs for understanding jet flow phenomena has been explored. Excitation of instabilities in the flow by LAFPAs results in a definitive

spatio-temporal origin to which resulting phenomena can be referenced. The absolute temporal reference afforded by LAFPA excitation provides researchers the ability to investigate the growth, saturation, and decay of structures with high fidelity. An example of their diagnostic potential can be found in the work of Kearney-Fischer *et al.* [citation], which investigated Mach wave radiation from heated, high Mach number jets using schlieren imaging phase-locked to LAFPAs.

Unlike their passive counterparts (such as tabs or mechanical chevrons), or some other potential active flow control technologies (such as fluidic chevrons), LAFPAs control the shear layer development indirectly by exciting naturally occurring instabilities. The sharp velocity gradient in the jet shear layer (or, more precisely the inflection point produced by this sharp gradient) gives rise to the inviscid Kelvin-Helmholtz instability [citation] (sometimes simply referred to as the initial shear layer instability). This instability is broadband and scales with the local momentum layer thickness and jet exit velocity (θ/U_j) ; perturbations over a wide range of frequencies can be amplified, though the dominant frequencies are found to be on the order of $St_\theta = f\theta/U_j = 0.012$ for very thin boundary layers [Cohen and Wygnasnki?]. The Kelvin-Helmholtz instability then drives the development of the large-scale structures in the shear layer by amplifying fine-scale perturbations, ultimately causing them to roll-up into coherent structures regardless of Reynolds number [Crow and Champaign, Brown and Roschko]. Owing to the axisymmetry of the jet nozzle (i.e. that the initial shear layer wraps around and connects to itself), various azimuthal Fourier modes are unstable to perturbations (including both axisymmetric and higher order modes) [Cohen?].

The growth of the shear layer as it advects downstream ultimately dictates that the shear layer merges with itself; this location is referred to as the end of the potential core. A secondary instability, the jet column instability, manifests in axisymmetric jets and is related to the passage of large-scale structures through the end of the potential core. This instability scales with the jet exit diameter and jet exit velocity (D/U_j) and is broadband, with a dominant characteristic frequency of $St_D = fD/U_j = 0.3$. The relation of the jet column instability to the initial shear layer instability is not well understood. Kibens argued that the jet preferred frequency is related to the initial shear layer frequency by the number of pairings of large scale structures that occur before the end of the potential core (i.e. $f_n/f_p = 2^n$), as the frequency of the structures halves after each pairing process [Kibens]. Conversely, Petersen claims that the jet preferred mode is simply the initial shear layer instability at the end of the potential core, and that the appearance of a single dominant lengthscale for the axisymmetric mode is due not to a type of 'global' instability of the flow field, but to a cutoff at the end of the potential core of the axisymmetric instability [Petersen and Samet 1988]. Regardless, it is clear that the large-scale oscillations of the jet shear layer and potential core are ultimately the product of small-scale perturbations which are amplified by the initial shear layer instability.

LAFPAs achieve flow control by utilizing this relationship between the initial shear layer instability and the jet column instability. The localized plasma arc-filament produces a rapid, localized heating through the Joule effect, and a compression wave is formed [Utkin 2007]. Though these perturbations are spatially discrete, they quickly amplify into large-scale coherent structures with well-defined characteristic spatial,

temporal, and azimuthal frequencies. Thus, LAFPAs are able to control the development of the most energetic scales in the jet shear layer; large-scale, azimuthally-coherent structures can be generated when enhanced mixing and jet spreading are desired, or smaller-scale, less azimuthally-coherent structures when noise reduction is necessary. In the present work, the subsonic jet is excited by LAFPAs, though here the goal is diagnostic rather than immediate practical application. The well-defined frequencies and phase of the large-scale structures produced by LAFPA actuation serve as an excellent reference for data acquisition and post-processing (e.g. phase-locking and phase-averaging).

1.2.2 Lighthill's Acoustic Analogy

Lighthill [6] was the first to identify that, by using an isentropic assumption for the momentum transport in the Navier-Stokes equations (thereby assuming a constant ratio for the density variation and hence a constant sound speed), the governing equations for fluid dynamics could produce a propagating wave equation driven by a highly-complex source field,

$$\frac{\partial^2 \rho}{\partial t^2} - a_0^2 \nabla^2 \rho = \frac{\partial^2}{\partial x_i \partial x_j} T_{ij}. \tag{1.1}$$

T_{ij}, commonly referred to as *Lighthill's stress tensor*, comprises Reynolds stresses, viscous stresses, and entropy fluctuations, respectively:

$$T_{ij} = \rho u_i u_j - \sigma_{ij} + \delta_{ij} \left[(p - \bar{p}) - a_0^2 (\rho - \bar{\rho}) \right]. \tag{1.2}$$

Here, a_0 refers to the ambient speed of sound, δ_{ij} is the Kronecker delta, and an overbar ($\bar{\cdot}$) corresponds to a time-averaged quantity. As the wave operator is linear,

the solution to this equation can be formulated with the aid of Green's functions,

$$\frac{\partial^2 G}{\partial t^2} - a_0^2 \nabla^2 G = \delta(\tau - t)\delta(\mathbf{x}' - \mathbf{x}). \tag{1.3}$$

The solution to this (see Crighton *et al.* [cite]) is the deceptively simple spatial integration of the source field at retarded time (that is, it is accounting for the propagation delay from the source location to the observer):

$$\rho(\mathbf{x}, t) = \frac{1}{4\pi} \int_\Omega \frac{S(\mathbf{x}', t - |\mathbf{x} - \mathbf{x}'|/a_0)}{|\mathbf{x} - \mathbf{x}'|} d^3\mathbf{x}'. \tag{1.4}$$

Lighthill's derivation of what became known as the first acoustic analogy (which in fact was specifically tailored to his study of jet noise) reformed the study of aeroacoustics. As has been discussed by many authors before (see Goldstein 1974 for example), this equation describes the propagation of sound, through a quiescent medium, generated by quadrupole sources.

Theoretical work based on Lighthill's approach was successful in predicting some aspects of experimentally-observed jet noise. Namely, stochastic source models of quadrupoles (per the aeroacoustic community's understanding of jet turbulence at the time) predicted a far-field pressure intensity scaling of $I \sim U_j^8$ which agreed with experimental results from cold, subsonic jets at sideline angles [Viswanathan]. However, this scaling law does not hold when the jet is heated or at low angles with respect to the jet exit, necessitating more complex source models. Later researchers (e.g. Goldstein [cite] and Lilley [cite]) further refined Lighthill's approach; providing successively clearer characterizations of the source physics. In addition to the true noise sources, Lighthill's acoustic source term includes flow-acoustic interactions, which describe diffraction and convection effects rather than true sources of noise. In a slightly different vein, analytical decompositions have been performed in order to separate the

disparate fluid phenomena inherent in Lighthill's source term and identify the roles of each [cabana 2008]. Unfortunately, given the complexity of the source field, even modern experimental techniques cannot acquire the full source with sufficient spatial and temporal fidelity to elucidate the flow structures responsible for the dominant noise emission.

1.2.3 The Role of Large-Scale Structures

Early work...(introduce stochastic models briefly, talk about coherent structures?)

Following the identification of coherent structures in turbulent jet shear layers [Mollo-christensen, crow, brown and roshko], source term models based on coherent eddies have frequently been employed, to varying degrees of success. A simplified model of the noise generation process in stationary free jets can be found in Fig. 1.1. This model is based off of the work of Tam *et al.* [1, 3], who observed that the far-field spectra could be represented as a combination of two similarity spectra based on polar angle of the observer, regardless of jet Mach number or temperature. At observer angles close to the jet downstream axis, the spectra exhibited a clearly defined spectral peak (F-spectrum), whereas at sideline or upstream angles the spectra were broadband (G-spectrum). From this observation the two-component acoustic source model was born: the isotropic fine-scale turbulence, dominant in the near-nozzle region, is responsible for the omni-directional acoustic radiation that dominates the sideline and upstream polar angles. On the other hand, the large-scale turbulent structures which exist further downstream produce the superdirective radiation that is readily apparent at aft polar angles.
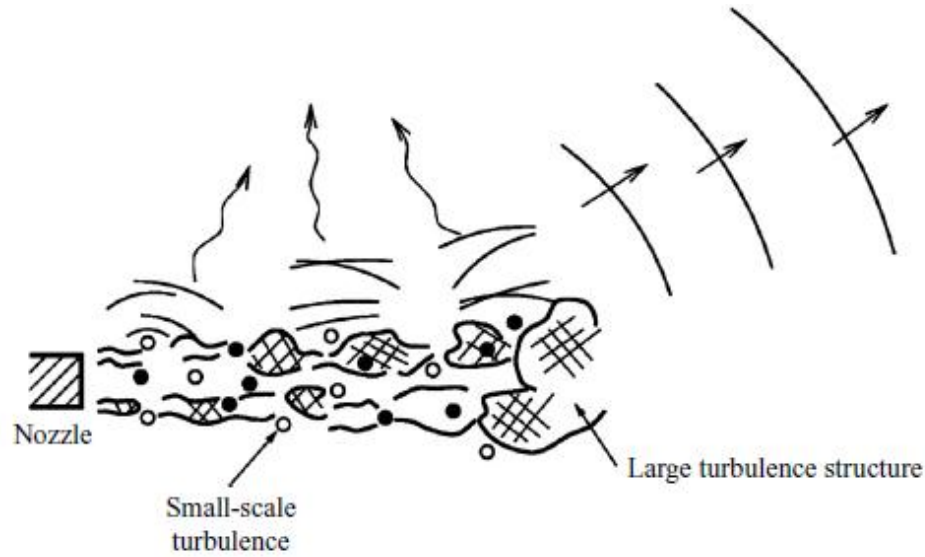
Figure 1.1: Simplified diagram of jet noise sources [TEMPORARY PLACE-HOLDER].

This model for ???, the so-called 'mixing noise' generated by both subsonic and supersonic jets ???

[Wavepacket models???]

Additional noise source mechanisms have been identified for supersonic jets. In imperfectly expanded jets, shock cells are produced in the jet. As turbulent structures pass through these waves, the sharp pressure gradients cause them to emit acoustic radiation. This is observed directly in the far-field as a broad-band amplification at high frequencies, referred to simply as broad-band shock-associated noise (BBSAN). In stationary or subsonic airframes this radiation can generate a feedback loop, whereby the noise travels upstream to the nozzle exit, excites the initial shear layer, and produces new structures at the same frequency. A high-amplitude, narrow-band tone (screech noise) is the end result of this feedback loop. Lastly,

supersonically-convecting (relative to the ambient) large-scale structures (which exist in supersonic and heated jets) produce high-amplitude, strongly-directional acoustic radiation towards aft angles. This Mach wave radiation can be explained by a wavy-wall analogy (Tam again?). In the present work, the jet is unheated and subsonic; as such these noise sources are not present and therefore neglected throughout the rest of this work.

Chapter 2: Experimental Methodology

2.1 Anechoic Chamber

All experiments were conducted at the GDTL within the Aerospace Research Center at the Ohio State University. Compressed, dried, and filtered air is supplied to the facility from two cylindrical storage tanks with a total capacity of 43 m^3 and maximum storage pressure of 16 MPa. The air may be routed through a storage heater, which allows the jet to operate with a stagnation temperature up to 500 °C, before expanding through a nozzle and exhausting horizontally into an anechoic chamber. As the current work was focused on a cold jet, the heater was rarely necessary; in certain circumstances though (namely, long experimental runs) the storage heater and bandheaters were used to slightly preheat the flow, thereby mitigating the temperature drop as the storage tanks were drained of high-pressure air. Opposite the nozzle, a collector accumulates the jet and entrained air and exhausts to the outdoors. A schematic of the anechoic chamber can be seen in Fig. 2.1. The dimensions of the chamber are 6.20 m wide by 5.59 m long and 3.36 m tall, with internal wedge-tip to wedge-tip dimensions of 5.14 m by 4.48 m and 2.53 m, respectively. The design of the chamber produces a cutoff frequency of 160 Hz, below the frequencies of interest for
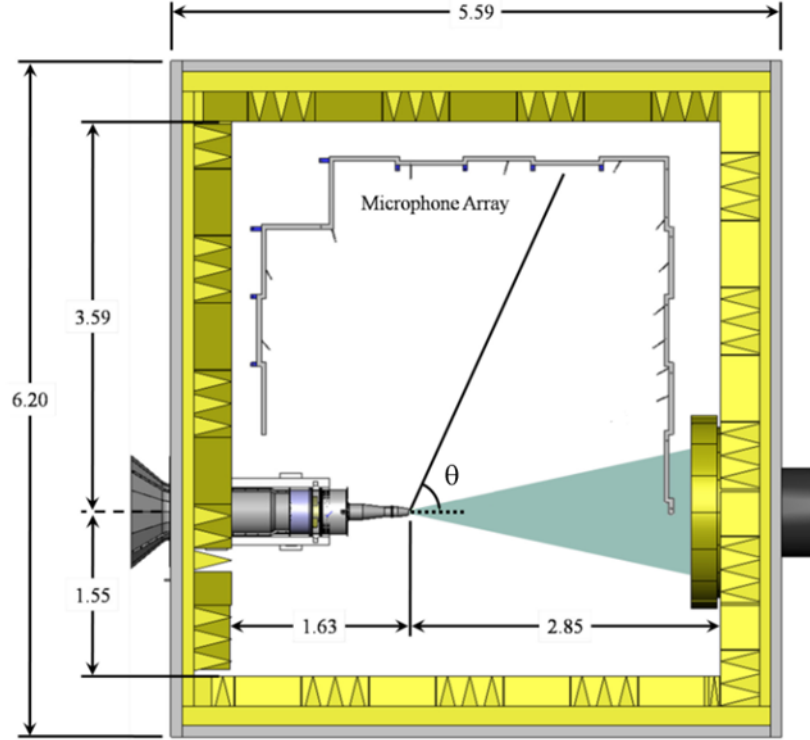
12

Figure 2.1: Top-down view of anechoic chamber and free jet facility at GDTL; dimensions are in meters.

this study. A more detailed description of the GDTL anechoic chamber properties and validation has been given by Hahn [cite].

For this study a converging, axisymmetric nozzle with exit diameter D of 25.4 mm was used. The internal contour of the nozzle was designed using a fifth order polynomial. The nozzle utilized a thick-lipped design in order to simplify the mounts for the LAFPA extension, which housed the eight actuators used in this study. For the experiments reported in this paper, the jet was operated at a Mach number (M_j) of 0.90, and with a total temperature ratio of approximately unity. The Reynolds number based on the jet exit diameter was 6.2×10^5; previous investigations using

hot-wire anemometry have indicated that the initial shear layer is turbulent for this operating condition with momentum thickness 0.09 mm and boundary layer thickness 1 mm [Kearney?].

2.2 Localized Arc-Filament Plasma Actuators

The design of the localized arc-filament plasma actuators, as well as the driving circuitry, has undergone a slow evolution since their initial development by the GDTL and NETL. In the current work, each LAFPA actuator consists of a pair of 1 mm diameter tungsten pin electrodes. The center-to-center spacing between electrode pairs for each actuator is 4 mm. Eight actuators were uniformly spaced around the nozzle perimeter 1 mm upstream of the nozzle exit. For electrical and thermal durability, the electrodes were housed in a boron nitride (grade AX05) extension attached to the end of the nozzle. A groove with dimensions of 1 mm wide and 0.5 mm deep is machined in the boron nitride, into which the electrode tips protrude, to provide a region of low momentum flow in order to stabilize the plasma arcs. It has been shown that the existence of this groove does not substantially alter the flow field or the control authority of the LAFPAs [Hahn]. A detailed description of initial development and LAFPA characteristics can be found in Utkin *et al.* [citation].

The LAFPAs were energized by a multi-channel, high-voltage plasma power generator capable of simultaneously powering up to eight LAFPAs, which was designed and built in-house at the GDTL. In this second-generation power supply, each individual circuit consists of a switchable capacitor in line with a high voltage transformer; the arcing electrodes are connected to the secondary side of the coil. The capacitor is charged by a 100 V DC power supply when the first switch is closed and the second is

opened; at the user-specified time the switches flip and it discharges through the coil. The switches are controlled by a 16-channel digital I/O card and National Instruments' Labview software, operated by a dedicated computer. The plasma generator provides independent control of the frequency, duty cycle/pulse width, and phase of each individual actuator (though not the amplitude). The pulse width was held constant at 7 s, which was found to be the minimum pulse width at which the actuators consistently arced for all frequencies explored in this study [citation]. The circuit is limited to 20 kHz due to thermal concerns. However, as the current work is focused on the evolution of large-scale structures (and ultimately their acoustic radiation), for which the dominant frequencies are on the order of 3 kHz, this is not an issue.

2.3 Data Acquisition

2.3.1 Near- and Far-field Pressure

Near-field and far-field pressure measurements were acquired using Brüel & Kjær 0.25-inch 4939 microphones and preamplifiers. The signal from each microphone is band-pass filtered from 20 Hz to 100 kHz using a Brüel & Kjær Nexus 2690 conditioning amplifier, and recorded using National Instruments PXI-6133 A/D boards and LabVIEW software. The microphones are calibrated using a Brüel & Kjær 114 dB, 1 kHz sine wave generator (type 4231). The frequency response of the microphones is flat up to roughly 80 kHz, with the protective grid covers removed.

Far-field acoustic pressure is acquired at three polar angles: 30, 60 and 90, as measured from the downstream jet axis. The positioning of the far-field microphone array can be seen in Fig. 2.1. The microphones were oriented such that they are at

normal incidence to the jet downstream axis at the nozzle exit. The radial distance of the microphones ranges from 101D at 30 to 145D at 60.

The near-field pressure was acquired during two separate experimental campaigns; the first focusing purely on the near-field and far-field pressure and the second focusing on the instantaneous velocity field. During the first campaign, the irrotational near-field was acquired using a linear array of sixteen microphones located along the meridional plane of the jet; the spacing varied along the array from 1D to 2D (see Fig. 2.2). The array was mounted on a two-axis linear traverse system the array and was inclined at an angle of 8.6° to the jet axis in order to match the spreading angle of the jet shear layer, as determined via PIV measurements during previous studies [28]. The traverse was controlled using LabView and enabled the acquisition of pressure measurements at various radial positions with respect to the jet axis. Initially, the most upstream microphone is positioned at x/D = 1 and r/D = 1.20, which is just outside the initial shear layer. For subsequent cases, the microphone array was incremented radially outward by 0.5D for a total travel distance of 7D, for a total of 15 array locations in the radial direction. Voltage signals were collected at 200 kHz with 81920 data points per block; sub-blocks of 8192 data points were used when calculating short-time power spectral densities, resulting in a frequency resolution of 24.4 Hz. Ten blocks were recorded for each case resulting in four seconds of data, which has been found to be sufficient for statistical convergence.

In the second experimental campaign, a shorter array consisting of 12 microphones equally space by $1D$ was used. In this case, the array was mounted from the floor and at an angle off the meridional plane of the jet (with microphone tips angled
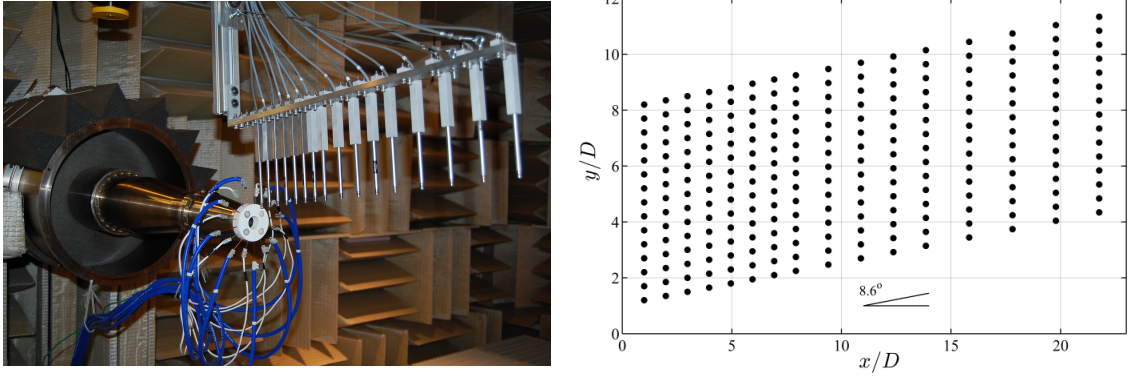
Figure 2.2: Photograph of anechoic chamber and nozzle, with near-field linear microphone array in foreground (a), schematic of all near-field microphone locations (b).

normal to the jet axis). This setup was used in conjunction with the particle image velocimetry described in the following section; the microphone array was placed off of the meridional plane so that it did not intersect with the laser sheet. As before, the microphone array was angled 8.6° with respect to the jet axis in order to match the spreading rate of the shear layer, and the axial and radial position was set to match the closest microphone array location used during the first experimental campaign. Voltage traces were acquired at 400 kHz, with 24576 points collected per block. The voltage traces were collected simultaneously with streamwise particle image velocimetry measurements; 1500 blocks were acquired, corresponding to the 1500 acquired images.

In addition to the microphone voltage traces, the acoustics data acquisition system recorded a reference signal corresponding to the LAFPA excitation. The TTL pulse sequence, which controls the LAFPAs, was supplied to an Agilent 3320A waveform generator. The rising edge of the TTL pulse triggered a sharp drop in the output

17

voltage of the waveform generator, which then ramps back up to the original voltage over a time interval which is shorter than the minimum excitation period. The output from the waveform generator was acquired simultaneously with the near- and far-field pressure signals using the aforementioned National Instruments hardware and software. As the excitation frequency, azimuthal mode, and ramp signal are well defined, this system enables the identification of the zero phase of actuation and hence, the ability to phase-average the pressure signals over the excitation period, akin to the work performed in Sinha *et al.* [citation]. This ensures that the seeded perturbations can be readily identified in the noisy flow, as well as allowing pressure signals, which were not recorded simultaneously (i.e. different near-field array positions), to be analyzed concurrently.

2.3.2 Particle Image Velocimetry

The instantaneous velocity was acquired using streamwise, two-component particle image velocimetry (PIV). A Spectra Physics, double-pulsed Nd:YAG laser (model PIV-400) was used as the illumination source. Due to facility requirements, the laser was located on a vibrationally-damped table outside the anechoic chamber and the laser beam was routed into the chamber using an overhead port; this resulted in a beampath of ~10 m. The laser sheet was formed using two cylindrical and one spherical lens; one of the cylindrical lenses was mounted to a rotational stage in order to ensure that the final laser sheet was normal to the jet exit (i.e. the laser sheet was streamwise to the jet). Alignment of the separate laser heads was initially performed using burn paper; final alignment was performed by seeding a low-velocity flow and visually checking that the same particles were captured in both frames. Per the best

18

practices explained in the LaVision DaVis manual, the timing between the two laser pulses was set so that particles in the jet core translated downstream by roughly half of the minimum correlation window width (16 pixels). For the present work, this resulted in a time delay of 3 μs. It was later observed that the actual time delay produced by the laser did not match the delay specified in the control software; this resulted in incorrect velocities being computed by the cross-correlations. In order to correct for this, the laser pulses were recorded using a ThorLabs DET210 photodetector and a LeCroy Wavejet 324A oscilloscope; the final vector fields were linearly scaled based on the ratio between the specified time delay and the measured time delay.

The jet core was seeded using Di-Ethyl-Hexyl-Sebacat (DEHS); the oil was atomized using a LaVision Aerosol generator and injected upstream of the turbulence screens in the stagnation chamber in order to produce a uniform seed particle density. As the jet entrains a significant amount of the surrounding ambient fluid as it evolves downstream, the coflow around the jet must also be seeded in order to accurately measure the outer shear layer velocity. For this, a TSI 6-jet atomizer (model 9306A) and olive oil was used; injection occurred into a plenum which surrounded the core stagnation chamber. Per the manufacturer's specfications, both atomizers provided nominally sub-micron seed particles. To ensure consistent seeding, this coflow was driven using a small Aerovent blower and a series of high-pressure ejectors. As a result, for the PIV data acquisitions, the jet core was surrounded by a ~5 m/s coflow.

Image groups were acquired using two LaVision Imager Pro SX 5M cameras, which had 12-bit resolution and 2560×2180 pixels. The combination of the PIV-400 laser and the Imager Pro SX cameras resulted in a maximum acquisition rate for the image

groups of 5 Hz. Nikon Nikkor 105 mm f/1.8 lenses were used, and 532 nm bandpass filters were mounted on the lenses. The cameras were positioned such that they were nominally normal to the image plane, negating the need for scheimpflug mounts. This was done as having high spatial resolution and field of view were deemed to be more important than having full, three-component velocity vectors. The cameras were aligned such that there was roughly a 10% overlap between the two images. This setup is generally designated as "side-to-side" in order to differentiate it from stereoscopic PIV; a schematic of the setup can be found in Fig. 2.3. The cameras were calibrated simultaneously using a LaVision calibration plate (type 31). Hardware background subtraction was used in order to reduce the effect of reflections off of the nozzle extension and near-field microphone array.

The image groups were acquired in two modes: ensemble and phase-locked. When in phase-locked mode, a reference signal from the LAFPA control computer was used as an external trigger for LaVision's DaVis software; various filters were placed inline in order to damp the electromagnetic interference generated by the LAFPAs. The reference signal was downsampled to roughly 10 Hz by the LAFPA control computer, and delayed appropriately in time to control the acquired actuation phase. For this case, 300 image groups were acquired for an individual phase. In ensemble mode, image groups were acquired randomly in time at the system's maximum acquisition rate (5 Hz). In this case, the PIV computer was set to output a reference signal which was used to trigger the acoustics data acquisition system. The timing was set such that the PIV image acquisition would occur roughly in the center of a data block acquired by the acoustics system; the signal from a ThorLabs DET210 photoreceiver was also recorded in order to accurately identify the timing of the image acquisition
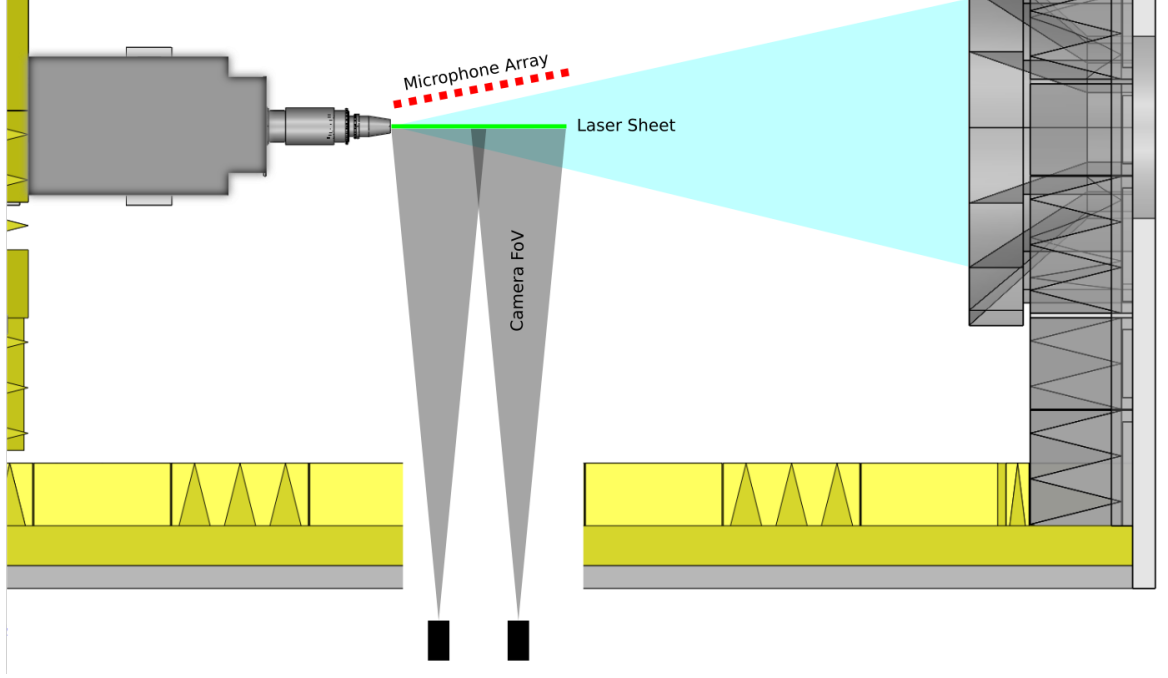
Figure 2.3: Schematic of syncronized PIV and near-field pressure data acquisition setup.

in relation to the pressure time traces. For this case, 1500 image groups were acquired for each case.

Instantaneous velocity vectors were computed using LaVision's DaVis software. Multipass, FFT-based cross-correlations were used, with decreasing window size ($64{\times}64$ for the initial pass, and $32{\times}32$ for the final three passes). A 50% overlap was used for the initial pass, and a 75% overlap was used for all subsequent passes. An gaussian window (elliptic in the streamwise direction) was applied to the correlation windows. The velocity fields were post-processed to remove spurious vectors, which were iteratively replaced if secondary correlation peaks were found, before the downstream and upstream images were combined. No interpolation, smoothing, or denoising was performed in post-processing.

Due to the nature of the plasma actuators used in these experiments (pulsed DC), electromagnetic interference (EMI) and radio-frequency interference (RFI) were significant concerns during data acquisition. Signal corruption could not only lead to excessively noisy data, but cause a mis-trigger event to occur between the laser, cameras, or microphones which would lead to garbage data. Great pains were therefore taken in order to isolate, shield and filter the electrical systems. A fiber-optic relay was designed and built in order to electrically isolate the plasma-generating equipment from the control computer (and ultimately the data acquisition systems). The plasma-generating equipment was also enclosed in a grounded metal rackmount cart to reduce the emitted RFI. Unfortunately, the building electrical grounds were also found to be corrupted by EMI, so additional filters were placed in stages along the trigger signal. A BenchMaster 21M Kemo filter, set to low-pass mode with a cutoff frequency of 99 kHz, was used to filter the flashlamp and q-switch trigger signals going into the laser power supply and head. Finally, between the LAFPA control computer and the PIV programmable timing unit input trigger a set of custom inductor-capacitor, resister-capacitor, and transient-voltage-suppressor filters were used.

Chapter 3: The Pressure Signature of Aeroacoustic Sources

Reference Ani's work here???

3.1 Preprocessing: Filtering the Actuator Self-Noise

Analysis of the near-field response of the forced jet is not immediately straightforward due to acoustic contamination from the actuators themselves [Kearney-fisher]. LAFPAs operate on a joule heating principle - the breakdown of the air between the electrodes and the ensuing flow of current results in intense heating of the air. This rapid, localized thermal perturbation produces a compression wave, which excites the shear layer. However, this compression wave is still evident as it travels through the near field. Multiple compression waves can clearly be seen in Fig. 3.1, in which a subsonic rectangular jet is being excited at 20 kHz by four LAFPAs on its lower edge.

Obviously, this is an undesirable effect, as this actuator self-noise may in some cases obscure the hydrodynamic and acoustic response of the jet. So, in the present work the near-field pressure signals have been preprocessed using a continuous-wavelet-based filtering algorithm, which has been specifically designed to remove the actuator self-noise while leaving the signature of the jet response unaltered. An example of this filtering can be found in Fig. 3.2, where the raw and preprocessed signals have been
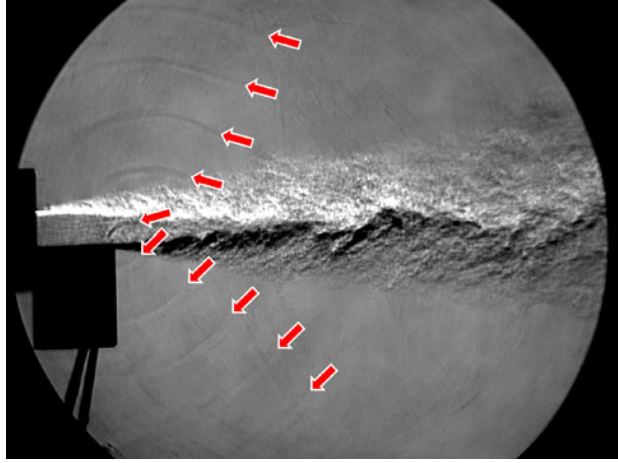
Figure 3.1: Schlieren image highlighting LAFPA compression waves. Reprinted from Samimy 2010 JFM.

plotted for $St_{DF} = 0.02$ at $x/D = 1$, $r/D = 1.20$. To aid in visualization, the results for multiple excitation periods has been phase-averaged to produce these waveforms. As the actuator self-noise is localized in both time and frequency and can be well predicted, a smoothing algorithm in the wavelet domain was found to be the most effective method for removing the undesirable noise while leaving the response of the jet intact. A fourth-order Paul wavelet is employed, due to the similarity of its imaginary component to the phase-averaged response of the jet. As a result, the energy of the response of the jet is well defined in the wavelet domain, with the actuator self-noise existing as high-frequency, temporally-localized oscillations superimposed on the field. After smoothing in the wavelet domain to remove these oscillations, the signal is transformed back into the physical domain where it undergoes another smoothing operation in order to remove small amplitude, high frequency oscillations which may be introduced by the wavelet-smoothing. For consistency hereafter, all
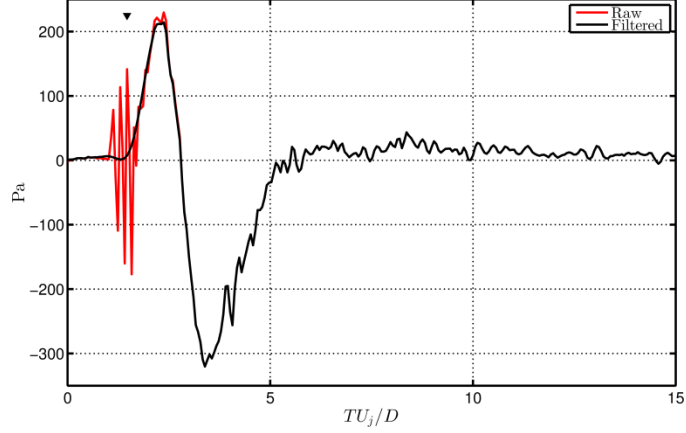
Figure 3.2: Raw and preprocessed near-field pressure.

results examined within this work have been computed from the filtered, rather than the raw, signals.

3.2 Far-field Response

3.3 Acoustic/Hydrodynamic Decomposition

Much of the difficulty in identifying the aeroacoustic source terms revolves around the dissimilar range of scales and fluctuation intensities of the turbulent eddies in the shear layer and the resulting radiated noise. Outside the jet shear layer, in the irrotational near-field of the jet, strong hydrodynamic pressure fluctuations associated directly with the passage of coherent structures in the shear layer and their resultant weak acoustic radiation coexist [Arndt]. Beyond this, in the acoustic far-field, the hydrodynamic signature of the coherent structures is nonexistent owing to their strong exponential decay with radial distance. It is in the irrotational near-field that much work has focused, in order to improve the aeroacoustic communitys understanding of the link between shear layer turbulence and far-field acoustic radiation.

25

Owing to the presence of strong hydrodynamic fluctuations dominating the irrotational pressure field near the noise source regions, identification of pure acoustic waves and their corresponding source events is problematic. A decomposition of the pressure field into its constitutive hydrodynamic and acoustic components is therefore required. By identification and prediction of coherence nulls in the near field, Coiffet *et al.* [cite] showed that the full irrotational near-field consistent primarily as a linear superposition of its hydrodynamic and acoustic components, which lead subsequent researchers to propose linear filters to extract the individual components from the near-field pressure, with varying degrees of success.

As discussed by Tinney & Jordan [cite], in a transonic jet in which the large-scale structures are convecting subsonically with respect to the ambient speed of sound, a demarcation of the hydrodynamic and acoustic energy fields can be observed with phase velocity. This is because the hydrodynamic pressure fluctuations will be aligned with the jet axis, and travelling subsonically. Acoustic pressure fluctuations will impinge on the linear microphone array at oblique angles, and therefore will appear as having either sonic or supersonic phase velocity, based on the source location. Therefore, a demarcaction between the hydrodynamic and acoustic energy components should be readily identifiable about the sonic wavenumber, $k_a = \omega/a_\infty$.

An illustration of this can be found in Fig. 3.3, where the power spectral density of the irrotational near-field pressure for a single microphone array position has been plotted as a function of normalized frequency and (axial) wavenumber. The sonic velocity has been identified with a dashed line; energies lying above this line correspond to supersonically traveling waves (and hence, acoustic energy) whereas energies below this line correspond to subsonically convecting waves (hydrodynamic energy). Note

that at high wavenumber and frequencies, two distinct energy lobes become readily apparent.

This phase-velocity separation is the basis for the decomposition method of Tinney & Jordan [cite], which used a Fourier-based wavenumber-frequency filter in a cold, subsonic jet to separate the near-field pressure into supersonically- and subsonically-convecting waves. The pressure field is first transformed into Fourier space (k_x, ω), as

$$\hat{p}(k_x, \omega) = \iint_{\mathbb{R}^2} p(x,t)e^{-i(\omega t - k_x x)}dxdt \tag{3.1}$$

From the transformed pressure field, the hydrodynamic and acoustic fields can then be reconstructed separately, from

$$p_c(x,t) = \frac{1}{(2\pi)^2} \iint_{\mathbb{R}^2} \phi_c(k_x, \omega)\hat{p}(k_x, \omega)e^{i(\omega t - k_x x)}dk_x d\omega. \tag{3.2}$$

The component weight vector, $\phi_c \in [0,1]$, is set based on the measured axial phase velocity, $c = \omega/k_x$ in order to filter out either the supersonic or subsonic portion of the spectra.

Grizzi & Camussi [cite] took a slightly different approach, which utilized a discrete wavelet transform at individual spatial locations in order to decompose the fields based on an energy cutoff. The energy threshold was set iteratively, using analysis of two-point correlations of the acoustic and hydrodynamic components between two microphones, in order to ensure that realistic phase-velocities for the components were met. The Empirical Mode Decomposition (EMD) based method of Kuo *et al.* [cite] dispensed with explicit concerns with the phase velocity of the pressure components and instead used the critical frequency, as defined by Arndt *et al.* [cite], which
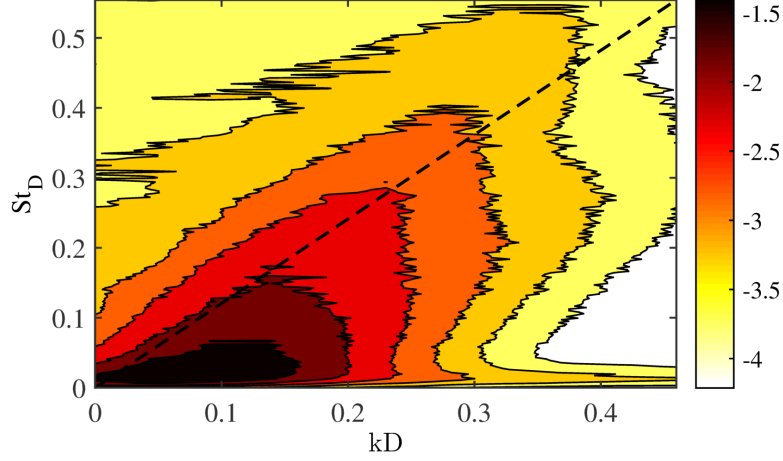
Figure 3.3: Wavenumber-Frequency spectral energy.

demarcates the energy dominance of the acoustic and hydrodynamic components in the near-field spectra. [Include recent Yonglu paper?]

In the current work, the irrotational near-field pressure is decomposed into its constitutive hydrodynamic and acoustic components based on phase-velocity. The current method is similar to that of Tinney & Jordan [cite] in that an axial array of many microphones is used, though it differs in how it identifies components of different phase-velocity. Here, the filtering will be performed by a spatio-temporal continuous wavelet transform.

3.3.1 The Wavelet Transform

Fourier analysis is commonly employed in the aeroacoustics community to study fundamental aspects of jet noise due to its simplicity and the great abundance of information it can provide. However, there is also a great drawback associated with Fourier analysis: while it analyzes a given signal at a distinct frequency, local information for a given event is spread over all spectral coefficients. This is due to the

28

fact that the basis functions used by the Fourier transform oscillate indefinitely. For a completely stationary signal this is not an issue, however it has become increasingly clear that the jet noise phenomenon is not a stationary process. Transient events, such as intermittency or the spatial and temporal modulation of a wavepacket, have been shown to be important in the noise generation process.

Grossman [cite] introduced the wavelet transform in an effort to overcome some of the shortcomings of the Fourier transform. Unlike the Fourier transform, the wavelet transform involves a convolution of the signal with a set of basis functions which decay to zero at the bounds. As a direct result, translation of the basis function in space and/or time is now meaningful. The basis functions (often referred to as the analyzing or daughter wavelets) are all derived from a single function, the mother wavelet, which must satisfy certain criteria [Farge], Most notable of of these criteria is that of admissibility, which in essence requires that the wavelet must be of finite energy. In practice, it is also helpful to choose a mother wavelet which is well-localized in both the spatio-temporal domain and the frequency domain. For a given mother wavelet, $\psi(\vec{x})$, the daughter wavelets can be constructed as

$$\psi_d\left(\vec{x}; s, \vec{\tau}, \theta\right) = s^{-n/2}\psi\left(s^{-1}r_{-\theta}\left(\vec{x} - \vec{\tau}\right)\right) \tag{3.3}$$

where s is the scale factor, $\vec{\tau}$ the translation parameter, and in the case of a multidimensional transform, $r_{-\theta}$ is the rotation vector (which can be neglected for an isotropic mother wavelet). The $s^{-n/2}$ factor ensures constant energy across all dilations. For a specific scale, translation, and rotation, the wavelet transform then becomes

$$\tilde{f}\left(s, \vec{\tau}, \theta\right) = \int_{\mathbb{R}^n} f\left(\vec{x}\right)\psi_d^*\left(\vec{x}; s, \vec{\tau}, \theta\right) d^n\vec{x}. \tag{3.4}$$

29

Because the basis functions of the wavelet transform are of finite energy, the locality of information in the original signal is preserved in the wavelet coefficients. This allows the identification, analysis, and reconstruction of localized events in the original signal, something not possible with the Fourier transform, which spreads temporal/spatial information over all transform coefficients. This has enabled previous researchers to perform a range of new analysis techniques to turbulence and acoustic phenomena not possible with the traditional Fourier transform. An excellent review of the development of wavelet analysis as well as applications to turbulence can be found in Farge [cite].

Use of a multidimensional, continuous wavelet transform to extract intermittent events with a specific phase-velocity is not immediately straightforward, due to the global nature of the scale factor. A 'speed-tuning' parameter, c, was introduced to the wavelet transform (now specifically referred to as a *spatio-temporal* wavelet transform) by Antoine *et al.* [cite], who used it for use in motion tracking and identification in two-dimensional images. The definition for the daughter wavelets (3.3) is modified to

$$\psi_d\left(\vec{x}, t; s, \vec{x}', t'\right) = s^{-n/2} \psi\left(s^{-1} c^{-1/n}(\vec{x} - \vec{x}'), s^{-1} c^{(n-1)/n}(t - t')\right) \qquad (3.5)$$

where n corresponds to the total number of dimensions (temporal and spatial).

The continuous wavelet transform are isometry [Antoine] and hence is invertible. The original signal may therefore be recovered from the wavelet coefficients as

$$f(\vec{x}, t) = \frac{1}{C_\delta} \int_0^\infty \frac{ds}{s^{1+n/2}} \int_0^\infty \frac{dc}{c} \tilde{f}(\vec{x}, t, s, c). \qquad (3.6)$$

The constant factor C_δ serves as an energy scaling, and appears because we are reconstructing the signal using a different analyzing wavelet (in this case, a delta function) than the mother wavelet used in the forward transform [Torrence,Farge,Antoine].

For a given mother wavelet, this factor can be found from

$$C_\delta = \frac{1}{(2\pi)^n} \int_0^\infty \frac{ds}{s^{1+n/2}} \int_0^\infty \frac{dc}{c} \int_{\mathbb{R}^{n-1}} d\vec{k} \int_{-\infty}^\infty d\omega \hat{\psi}_d^* \quad (3.7)$$

where $\hat{\psi}_d$ are the daughter wavelets in Fourier space. Since we are interested in decomposing the field into the acoustic and hydrodynamic components, a filtered reconstruction can be done quite easily in the wavelet domain by simply modifying the integration limits in Eqn. 3.6 to include only speed-tuning parameters corresponding to the subsonic or supersonic portion of the wavelet spectrum.

In this way, this methodology can be thought of as a simple modification of that proposed by Tinney & Jordan [cite], replacing the Fourier transform in their method with a spatio-temporal wavelet transform. The relationship between the wavelet transform and the Fourier transform can be further elucidated by computing the forward transform in the Fourier domain (with the use of the convolution theorem), inserting this into Eqn. 3.6, and reversing the order of the integration:

$$f_c(\vec{x}, t) = \frac{1}{(2\pi)^n} \int_{\mathbb{R}^{n-1}} d\vec{k} \int_{-\infty}^\infty d\omega \hat{f}(\vec{k}, \omega) e^{i(\omega t - \vec{k}\cdot\vec{x})}$$

$$\times \frac{1}{C_\delta} \int_0^\infty \frac{ds}{s^{1+n/2}} \int_0^\infty \frac{dc}{c} \hat{\psi}_d^*(sc^{1/2}k, sc^{-1/2}\omega) \quad (3.8)$$

$$f_c(\vec{x}, t) = \frac{1}{(2\pi)^n} \int_{\mathbb{R}^{n-1}} d\vec{k} \int_{-\infty}^\infty d\omega \hat{f}(\vec{k}, \omega) e^{i(\omega t - \vec{k}\cdot\vec{x})} \phi_c(k, \omega) \quad (3.9)$$

The appearance of Eqn. 3.9 is identical to that of Eqn. 3.2; the difference lies in how filter ϕ_c is defined, either explicitly in the Fourier domain in the case of the Fourier filtering or implicitly by the shape of the chosen mother wavelet in the wavelet transform. As numerous other researchers have discussed, this leads to an alternative interpretation of the wavelet transform, that of a series of bandpass filters, the passband envelope, centroid, and width being dictated by the scale, speed, and mother wavelet [Farge, torrence].

In fact, computing the convolutions is much faster in the Fourier domain than in the physical domain, so Eqn. 3.9 is the preferred method for computing the spatio-temporal wavelet filter. The decompositions were performed along each radial microphone array position individually, using the (1+1) dimensional (space-time) Morlet wavelet as the mother wavelet:

$$\psi(x,t) = e^{i(k_o x + \omega_0 t)} e^{-(x^2 + t^2)/2} \tag{3.10}$$

which the reader will recognize as simply a plane wave modulated by a Gaussian. Though simplicity was a factor in this decision, previous results analyzing phase-averaged waveforms in the far-field found acoustic emissions with a characteristic waveform that share some resemblance to the Morlet wavelet [crawley2014]. The base oscillation frequencies, (k_0, ω_0) were set to $(\pm 5, 5)$ (the dual sign for k_0 being necessary to recover both forward and backward traveling waves), and $\hat{\psi}(k, 0) = 0$ and $\hat{\psi}(0, \omega) = 0$ so as to ensure that the mother wavelet met the admissibility criterion.

As the microphone array is irregularly spaced in the axial direction, the pressure field was interpolated onto a regular grid of spacing $1D$ before computation of the discrete Fourier transform. In the current work, the local speed of sound was chosen as the phase-velocity demarcation, as opposed to the ambient speed of sound which had been used by previous researchers [Tinney and Jordan]. In our case, the jet under study is subsonic and unheated, meaning that the local speed of sound (320 m/s) is still greater than the jet velocity (287 m/s) yet lower than the ambient speed of sound (346 m/s) and hence is a better choice for this particular application.
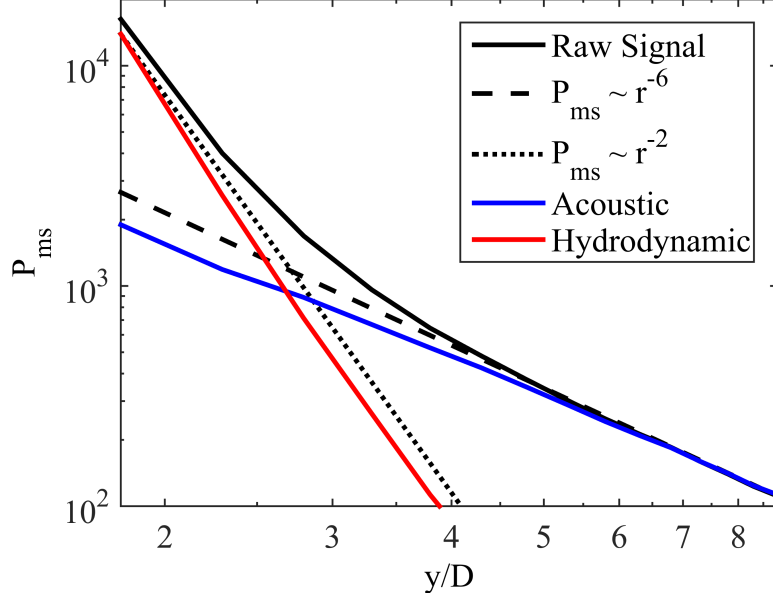
Figure 3.4: Radial decay of the raw signal compared against the theoretically-obtained and experimentally-measured decay rates for the acoustic and hydrodynamic components.

3.3.2 Validation

Though broad in its view, a simple evaluation of the decomposition algorithm can first be made by examination of the radial decay of the pressure fluctuation intensities, as has been done in Fig. 3.4 at an axial position near the end of the potential core. Theoretical analysis by Ribner [cite] and Arndt *et al.* [cite] showed that the intensity of the full hydrodynamic field (as opposed to the inertial field alone) decays as $I \sim r^{-6}$. In contrast, the acoustic field has been shown to be well-approximated by the linearized Euler equations, which exhibit $I \sim r^{-2}$ decay rates (that is, the field is dominated by spherically propagating waves). Hence, the individually processed microphone array positions can serve as an initial validation step for the radial decay of the decomposed fields.
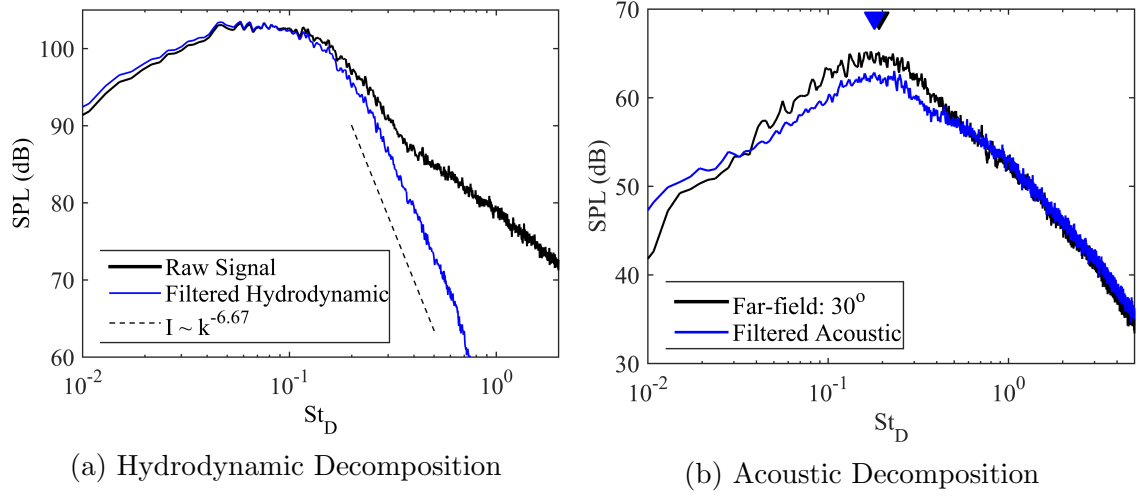
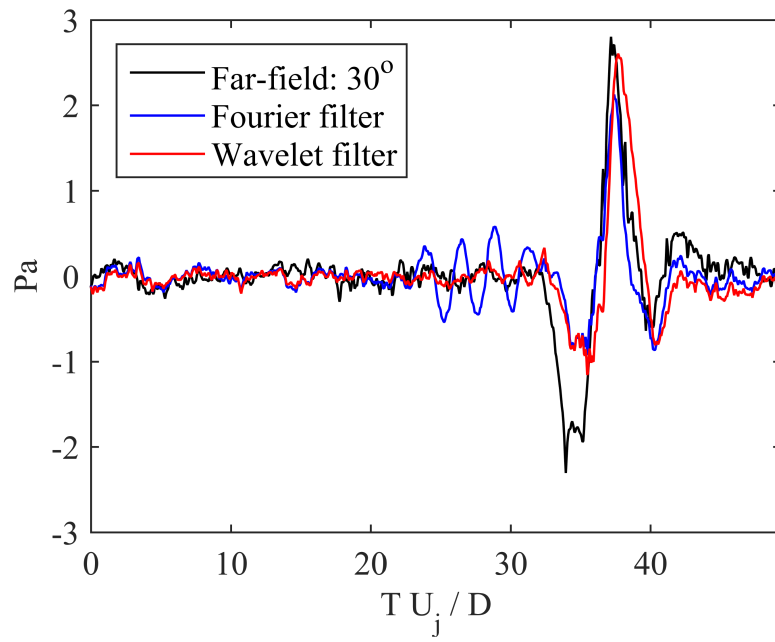(a) Hydrodynamic Decomposition

(b) Acoustic Decomposition

Figure 3.5: ???

Figure 3.6: ???

3.4 Identifying the Acoustic Source Region

Chapter 4: Estimation of Time-resolved Velocity Fields

4.1 Stochastic Estimation

4.1.1 Artificial Neural Networks

4.1.2 Validation

Chapter 5: Dilatation as the Aeroacoustic Acoustic Source

Chapter 6: Conclusions

Bibliography

[1] Christopher K. W. Tam, Golebiowski, Michel, and J. M. Seiner. On the two components of turbulent mixing noise from supersonic jets. In *2nd AIAA/CEAS Aeroacoustics Conference*, volume AIAA Paper, 1996.

[2] K Viswanathan. Scaling laws and a method for identifying components of jet noise. *AIAA Journal*, 44(10):2274–2285, 2006.

[3] Christopher K. W. Tam, K. Viswanathan, K. Ahuja, and J. Panda. The source of jet noise: Experimental evidence. *Journal of Fluid Mechanics*, 615:253–292, 2008.

[4] Marie Cabana, Vronique Fortun, and Peter Jordan. Identifying the radiating core of lighthill's source term. *Theoretical Computational Fluid Dynamics*, 22:87–106, 2008.

[5] P. Jordan and Y. Gervais. Subsonic jet aeroacoustics: associating experiment, modelling and simulations. *Experiments in Fluids*, 44:1–21, 2008.

[6] M. J. Lighthill. On sound generated aerodynamically. i. general theory. In *Proceedings of the Royal Society of London: Series A, Mathematical and Physical Sciences*, volume 211, pages 564–587. The Royal Society, 1952.